Journal of Marine Science and Technology

Volume 27 | Issue 1 Article 3

ROBUST SUPER-RESOLUTION APPROACH TO SOURCE LOCALIZATION IN OCEAN WAVEGUIDE USING SPARSITY CONSTRAINT

Hai-Yan Song
School of Electrical and Information Engineering, Heilongjiang Institute of Technology, Harbin, China

Chang-Yi Yang
Department of Computer Science and Information Engineering, National Penghu University of Science and Technology, Magong 880, Taiwan, R.O.C, songhaiyan0508@hrbeu.edu.cn

Ke-Jun Wang
Swanson School of Engineering, Department of Bioengineering, University of Pittsburgh, 3700 O'Hara Street, Pittsburgh, PA 15260 USA.

Recommended Citation
Song, Hai-Yan; Yang, Chang-Yi; and Wang, Ke-Jun (2019) "ROBUST SUPER-RESOLUTION APPROACH TO SOURCE LOCALIZATION IN OCEAN WAVEGUIDE USING SPARSITY CONSTRAINT," *Journal of Marine Science and Technology*: Vol. 27: Iss. 1, Article 3.
DOI: 10.6119/JMST.201902_27(1).0003
Available at: https://jmstt.ntou.edu.tw/journal/vol27/iss1/3

ROBUST SUPER-RESOLUTION APPROACH TO SOURCE LOCALIZATION IN OCEAN WAVEGUIDE USING SPARSITY CONSTRAINT

Acknowledgements

This work was supported by the Fund for Young Fostering Talents of the Higher Education Institutions in Heilongjiang Province in 2015 (Grant No. UNPYSCT-2015101), the Natural Science Foundation for Outstanding Young Talents of Heilongjiang Province and the Fundamental Research Funds for the Universities of Education Department of Heilongjiang Province (Innovative Research Team: Grant No. 2018CX11).

Journal of Marine Science and Technology, Vol. 27, No. 1, pp. 17-27 (2019)
DOI: 10.6119/JMST.201902_27(1).0003

ROBUST SUPER-RESOLUTION APPROACH TO SOURCE LOCALIZATION IN OCEAN WAVEGUIDE USING SPARSITY CONSTRAINT

Hai-Yan Song[1], Chang-Yi Yang[2], and Ke-Jun Wang[3]

Key words: source localization in ocean waveguide, compressive sensing, sparsity constraint, matched-field processing.

ABSTRACT

Source localization in an ocean waveguide is a challenging problem because of the complexity of underwater acoustic propagation. Matched-field processing (MFP) has attracted considerable attention and has become a crucial technique for underwater acoustic source localization. Compressive sensing can achieve spatial sparsity, thus improving spatial resolution, by imposing penalties based on l_1-norm. In this study, we developed a robust super-resolution approach for source localization in an ocean waveguide, which utilizes the inherent sparse structure of the spatial localization problem and underwater sound propagation principle. The proposed approach can be formulated as a sparse representation problem and further converted into a convex optimization problem with sparsity constraints. Moreover, the approach can be easily implemented and efficiently solved using currently available convex optimization software toolboxes based on interior point algorithms, such as CVX. The approach can also be extended to multiple-measurement scenarios for achieving superior source localization performance. In addition, the effect of the signal-to-noise ratio (SNR), a constraint parameter, and model mismatch on source localization performance was thoroughly analyzed using computer simulations. Numerical simulation results demonstrated that in some challenging scenarios, the proposed approach exhibited superior performance compared with existing conventional methods, such as a low source localization error and high mainlobe-to-sidelobe ratio.

Paper submitted 06/07/18; revised 08/20/18; accepted 12/19/18. Author for correspondence: Chang-Yi Yang (e-mail: songhaiyan0508@hrbeu.edu.cn).
[1] School of Electrical and Information Engineering, Heilongjiang Institute of Technology, Harbin, China.
[2] Department of Computer Science and Information Engineering, National Penghu University of Science and Technology, Magong 880, Taiwan, R.O.C.
[3] Swanson School of Engineering, Department of Bioengineering, University of Pittsburgh, 3700 O'Hara Street, Pittsburgh, PA 15260 USA.

I. INTRODUCTION

In array signal processing, source localization has become an active research area with applications in radar, sonar, electromagnetic, medical imaging, and other fields (Chang et al., 2001; Hou et al., 2009; Jiang et al., 2017a). Among such applications, underwater acoustic source localization in an ocean waveguide is a particularly challenging task in underwater acoustics (Shi et al., 2011c; Dosso and Wilmut, 2013; Song et al., 2015; Jiang et al., 2017b).

Over the past 50 years, matched-field processing (MFP), which is a natural extension of classical plane wave beamforming to an ocean waveguide, has attracted considerable attention and has become a crucial technique for underwater acoustic source localization (Kuperman and Song, 2012). However, although MFP is considerably more advanced than simple plane wave processing, it is evidently not perfect. A primary limitation is the presence of sidelobes in Ambiguity Surface (AMS), and another limitation can be its lack of resolution, particularly with regard to source depth. To improve the performance of conventional MFP, numerous alternate approaches have subsequently been developed. One of these approaches is the minimum-variance (MV) processor, which can strongly suppress sidelobes and has a considerably sharper and more focused peak at the accurate source localization than do other processors (Tolstoy, 1993). Nevertheless, the MV processor also has disadvantages (Shi et al., 2011a; Somasundaram et al., 2015). In particular, it experiences severe performance degradation in the presence of errors in the model estimates of the field and under mismatch conditions (Shi et al., 2012). Because of this sensitivity, quantitative knowledge of environmental parameters must be extremely detailed and accurate (Shi et al., 2011b).

Compressive sensing or compressive sampling (CS) is a novel sensing/sampling paradigm that is against the conventional sampling rate (the so-called Nyquist rate) and marks the beginning of a new era in the data acquisition literature (Candes and Wakin, 2008; Orović et al., 2016). With the rapid development in both theory and algorithms for sparse recovery in finite dimensions, compressive sensing has become an appealing field that has attracted considerable attention in the signal processing domain (Li and Zhang, 2015; Zhang et al., 2015). Moreover, the broad

applicability of the CS framework has motivated notable studies in source localization (Rossi et al., 2014; Si et al. 2015).

Through the CS framework, the inherent sparsity of underlying signals in space domains can be capitalized upon to achieve super-resolution localization in a noisy and coherent environment with few snapshots (Bilik, 2011; Yin et al., 2016). Malioutov et al. (2005) enforced sparsity by imposing penalties based on l_1-norms and used the singular value decomposition of a data matrix to improve the performance of CS in direction-of-arrival (DOA) estimation. Gorodnitsky and Rao (1997) considered DOA estimation as an underdetermined problem and used a recursive weighted minimum-norm algorithm termed focal underdetermined system solver (FOCUSS) to determine its sparse solutions.

In ocean acoustics, Xenaki et al. (2014) thoroughly analyzed the performance of CS in DOA estimation, particularly in challenging scenarios, such as those involving coherent arrivals and single-snapshot data; they finally demonstrated the high-resolution capabilities and robustness of CS on experimental array data. Edelmann and Gaumond (2011) applied CS to the beamforming of measured underwater acoustic data from the BASE07 experiment and showed that compressive beamforming has finer angular resolution and greater interference suppression than does conventional beamforming. Additionally, CS was introduced to considerably mitigate the computational workload by "compressing" these computations of MFP (Mantzel et al., 2012). Forero and Baxley (2014) presented a robust scheme for shallow-water source localization that utilizes the inherent sparse structure of the localization problem, and they developed an iterative solver based on block-coordinate descent.

Research has established CS as a valuable tool for source localization; however, research has primarily established this from a plane-wave perspective, seldom considering an ocean waveguide. Therefore, the aim of this study was to achieve superior resolution and suppressed sidelobes by introducing a spatial-sparsity constraint into shallow-water source localization. In contrast to the study by Mantzel et al. (2012), we used sparsity to improve source localization performance and did not address the computational challenges of computing replicas for large grids. Moreover, unlike the study by Forero and Baxley (2014), we formulated the underwater source localization problem as a convex optimization problem and applied the CVX tool to efficiently solve nondifferentiable functions (l_1-norms) in both single- and multiple-measurement scenarios. The primary contributions of this study are as follows: (1) formulating the source localization problem in an ocean waveguide as a sparse representation problem and converting this problem into a convex optimization problem with a sparsity constraint, which can be efficiently solved using the well-established toolbox CVX; and (2) extending a single-measurement algorithm to a multiple-measurement scenario and achieving superior source localization performance, including robustness against model mismatch.

The remainder of this article is organized as follows: Section II presents preliminary information on CS, and the sparse signal recovery algorithm is considered in this section. In Section III, underwater acoustic propagation theory in an ocean waveguide is introduced, and the traditional MFP techniques are described. In Section IV, the source localization problem in an ocean waveguide is reformulated as a sparse representation problem, and the source localization algorithm with a sparsity constraint in the ocean waveguide is then proposed. Section V presents a detailed analysis of numerical results by using synthetic data. The conclusions are provided in Section VI.

II. CS PROBLEM AND SPARSE SIGNAL RECOVERY ALGORITHM

CS is a novel sensing/sampling paradigm that entails capturing and representing compressible signals at a rate that is significantly below the Nyquist rate (Eldar and Kutyniok, 2012). In general, several natural signals can be expressed in a convenient orthonormal basis. For example, any signal $\mathbf{x} \in \mathbf{R}^N$ (where $\mathbf{R}^N$ represents an N-dimensional Euclidean space and N is the corresponding dimension) can be expanded in an orthonormal basis $\mathbf{\Psi} = \left[\mathbf{\Psi}_1, \mathbf{\Psi}_2, \ldots, \mathbf{\Psi}_N\right]$ as follows:

$$\mathbf{x} = \sum_{i=1}^{N} s_i \boldsymbol{\psi}_i \text{ or } \mathbf{x} = \mathbf{\Psi}\mathbf{s} \tag{1}$$

where $\mathbf{s}$ denotes the coefficient sequence of $\mathbf{x}$, $s_i = \langle \mathbf{x}, \boldsymbol{\psi}_i \rangle = \boldsymbol{\psi}_i^{\mathrm{T}} \mathbf{x}$, and $(\cdot)^{\mathrm{T}}$ denotes transposition. Clearly, $\mathbf{x}$ and $\mathbf{s}$ are equivalent representations of the signal, with $\mathbf{x}$ in the time or space domain and $\mathbf{s}$ in the $\mathbf{\Psi}$ domain.

The signal $\mathbf{x}$ is strictly *sparse* because almost all of its entries are zero. The signal $\mathbf{x}$ is *K-sparse* if it is a linear combination of at most K basis vectors. The signal $\mathbf{x}$ is *compressible* in that Eq. (1) has only a few large coefficients and several small coefficients (Baraniuk, 2007).

Consider a general linear measurement process that computes M inner products between $\mathbf{x}$ and a collection of vectors $\{\boldsymbol{\phi}_j\}_{j=1}^{M}$ as follows:

$$y_j = \langle \mathbf{x}, \boldsymbol{\phi}_j \rangle \text{ or } \mathbf{y} = \mathbf{\Phi}\mathbf{x} \tag{2}$$

If Eq. (1) is substituted into Eq. (2), $\mathbf{y}$ can be written as follows:

$$\mathbf{y} = \mathbf{\Phi}\mathbf{x} = \mathbf{\Phi}\mathbf{\Psi}\mathbf{s} = \mathbf{\Theta}\mathbf{s} \tag{3}$$

where the sensing matrix $\mathbf{\Theta} = \mathbf{\Phi}\mathbf{\Psi}$ is the product of the measurement matrix $\mathbf{\Phi}_{M\times N}$ and the transformation matrix $\mathbf{\Psi}_{N\times N}$. Notably, M is a number and determines the number of vectors $\boldsymbol{\phi}_j$ (j = 1, …, M) used for generating a linear measurement process. In general, M is less than N; thus, Eq. (3) is underdetermined and does not have a unique solution. Moreover, Eq. (3) is a typical compressive sensing problem, which involves designing a reconstruction algorithm to recover $\mathbf{s}$ from

only M ≈ K measurements **y**.

The sparse signal recovery algorithm entails taking M measurements in the vector **y**, measurement matrix $\mathbf{\Phi}$, and transformation matrix $\mathbf{\Psi}$ to reconstruct the length-N signal **x** or equivalently its sparse coefficient vector **s**.

A classical approach to Eq. (3) is to determine the solution with minimum energy (l_2-norm) by solving the following:

$$\min \|\mathbf{s}\|_2 \quad s.t. \quad \mathbf{y} = \mathbf{\Theta s} \tag{4}$$

where *s.t.* denotes "subject to." The optimization problem Eq. (4) has a convenient analytical solution:

$$\mathbf{s} = \mathbf{\Theta}^{\mathrm{T}} \left(\mathbf{\Theta}\mathbf{\Theta}^{\mathrm{T}} \right)^{-1} \mathbf{y} \tag{5}$$

However, l_2-norm minimization aims to minimize the signal energy rather than its sparsity; hence, it almost never determines a K-sparse solution. By definition, an ideal measure of sparsity is to count the number of nonzero entries in **s**, which is mathematically termed l_0-norm (denoted by $\|\mathbf{s}\|_0$). Therefore, sparsity can be imposed on **s** by minimizing l_0-norm as follows:

$$\min \|\mathbf{s}\|_0 \quad s.t. \quad \mathbf{y} = \mathbf{\Theta s} \tag{6}$$

Eq. (6) is a difficult combinatorial optimization problem, and this problem is numerically unstable and NP-hard. In previous studies, numerous algorithms have been proposed, including greedy algorithms as well as l_1 and l_p relaxations (Donoho, 2006). For l_1 and l_p relaxations, recent research has proven that if the signals are sufficiently sparse with respect to a sensing matrix, Eq. (6) is equivalent to the following:

$$\min \|\mathbf{s}\|_1 \quad s.t. \quad \mathbf{y} = \mathbf{\Theta s} \tag{7}$$

This is a convex optimization problem, which can be reduced to a linear program termed basis pursuit, whose computational complexity is approximately $O(N^3)$ (Candès, 2006). Furthermore, because of the convexity of l_1-norm, the global optimum can be conveniently determined.

III. TRADITIONAL MFP FOR SOURCE LOCALIZATION IN OCEAN WAVEGUIDE

In underwater acoustics, acoustic propagation is described using a pressure disturbance or field traveling through the ocean, where the water medium and boundaries (the surface and the bottom) can vary temporally and spatially. The theoretical basis underlying all mathematical models of acoustic propagation is the wave equation, which is derived from the fundamental equations of state, continuity, and motion (Jensen et al., 2011; Schmidt and Jensen, 2012). With the maturation of modeling technology over previous decades, four types of propagation models are available, namely Ray theory, fast field program, parabolic equation, and normal-mode (NM) model (Tolstoy, 1993; Jiang et al., 2017). The principal advantages of the NM model include high-accuracy and rapid calculation. Therefore, the NM model is generally preferred for MFP. For consistency and simplicity, all results computed particularly for this study were generated using the NM model.

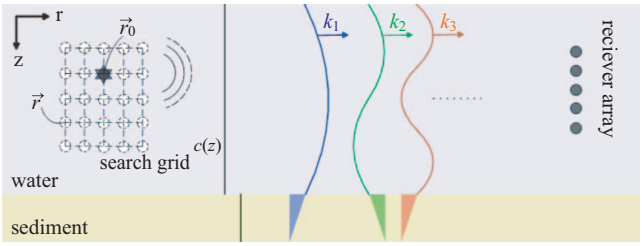

Fig. 1. Underwater acoustic propagation and MFP implementation in ocean waveguide.

The problem considered in this study involved calculating the response to an isotropic point source in a stratified acoustic medium, as indicated schematically in Fig. 1.

Within a layer, the solution is governed by the following acoustic wave equation:

$$\nabla \cdot \left(\frac{1}{\rho(z)} \nabla P \right) - \frac{1}{\rho(z) c^2(z)} P_{tt} = -s(t) \frac{\delta(z - z_s)\delta(r)}{2\pi r} \tag{8}$$

where $P(r, z, t)$ is the acoustic pressure as a function of depth z, range r, and time t. In addition, $c(z)$, $\rho(z)$, and $s(t)$ represent the sound speed, density, and isotropic point source, respectively.

Assume that $s(t)$ has only a single frequency component ω. The source time series can then be represented as follows:

$$s(t) = e^{-j\omega t} \tag{9}$$

which generates a pressure field with the same harmonic time dependence as follows:

$$P(r, z, t) = p(r, z) e^{-j\omega t} \tag{10}$$

Substituting Eqs. (9) and (10) into Eq. (8) yields the Helmholtz equation:

$$\frac{1}{r} \frac{\partial}{\partial r} \left(r \frac{\partial p}{\partial r} \right) + \rho(z) \frac{\partial}{\partial z} \left(\frac{1}{\rho(z)} \frac{\partial p}{\partial z} \right) + \frac{\omega^2}{c^2(z)} p = \frac{-\delta(z - z_s)\delta(r)}{2\pi r} \tag{11}$$

Using the technique of separation of variables and the boundary condition, we can derive the following (Etter, 2013):

$$p(r, z) \approx \frac{j}{\rho(z_s)\sqrt{8\pi r}} e^{-j\pi/4} \sum_{m=1}^{\infty} Z_m(z_s) Z_m(z) \frac{e^{jk_m r}}{\sqrt{k_m}} \tag{12}$$

where k_m and Z_m are the eigenvalue and eigenfunction, respectively. Furthermore, $p(r, z)$ is referred to as the Green's function $G(r, z)$, which forms the basis for representing signals used in MFP.

Fig. 1 presents a schematic of MFP implementation in an ocean waveguide. The acoustic source $s_0(t)$ (star symbol) is located at an unknown location $\vec{r}_0 = (r_0, z_{s0})$, and its transmitting signal is recorded along an N-element receiver array after multipath propagation. According to the aforementioned NM model, the solutions to the wave equation at the array locations are represented as $G(\vec{\mathbf{r}}_0, \vec{\mathbf{r}}_i)$, ($i$ = 1, …, N) ($\vec{\mathbf{r}}_i$ represents the location for the ith element), and can be incorporated into a signal vector $\mathbf{G}(\vec{\mathbf{r}}_0, \vec{\mathbf{r}}) = \left[G(\vec{\mathbf{r}}_0, \vec{\mathbf{r}}_1), G(\vec{\mathbf{r}}_0, \vec{\mathbf{r}}_2), \ldots, G(\vec{\mathbf{r}}_0, \vec{\mathbf{r}}_N)\right]^{\mathrm{T}}$ (where $\vec{\mathbf{r}} = [\vec{\mathbf{r}}_1, \vec{\mathbf{r}}_2, \ldots, \vec{\mathbf{r}}_N]$), which is the measured acoustic field on the vertical array. A modeled acoustic field for a candidate source located at $\vec{\mathbf{r}}_s = (r, z_s)$ can be denoted as $\hat{\mathbf{G}}(\vec{\mathbf{r}}_s, \vec{\mathbf{r}}) = \left[\hat{G}(\vec{\mathbf{r}}_s, \vec{\mathbf{r}}_1), \hat{G}(\vec{\mathbf{r}}_s, \vec{\mathbf{r}}_2), \ldots, \hat{G}(\vec{\mathbf{r}}_s, \vec{\mathbf{r}}_N)\right]^{\mathrm{T}}$. The actual source location $\vec{\mathbf{r}}_0$ may be inferred by matching the measured acoustic field $\mathbf{G}(\vec{\mathbf{r}}_0, \vec{\mathbf{r}})$ with the simulated acoustic signals $\hat{\mathbf{G}}(\vec{\mathbf{r}}_s, \vec{\mathbf{r}})$ obtained by varying the candidate source location (dot symbols) $\vec{\mathbf{r}} = (r, z_s)$ throughout a search grid area. MFP is a generalization of plane wave beamforming, wherein a steering vector (or replica) is derived from the Green's function of the ocean waveguide; therefore, the conventional MFP algorithm with the Bartlett processor can be formulated as follows (Baggeroer et al., 1993; Yang, 2014):

$$P_B(\vec{\mathbf{r}}_s, \vec{\mathbf{r}}) = \mathbf{w}^{\mathrm{H}}(\vec{\mathbf{r}}_s, \vec{\mathbf{r}})\mathbf{K}\mathbf{w}(\vec{\mathbf{r}}_s, \vec{\mathbf{r}}) \tag{13}$$

where $P_B(\vec{\mathbf{r}}_s, \vec{\mathbf{r}})$ represents the output power of the Bartlett processor, $\mathbf{w}(\vec{\mathbf{r}}_s, \vec{\mathbf{r}}) = \dfrac{\hat{\mathbf{G}}(\vec{\mathbf{r}}_s, \vec{\mathbf{r}})}{\left|\hat{\mathbf{G}}(\vec{\mathbf{r}}_s, \vec{\mathbf{r}})\right|}$ represents the normalized weight vector, $\mathbf{K} = \left\langle \mathbf{G}(\vec{\mathbf{r}}_0, \vec{\mathbf{r}})\mathbf{G}^{\mathrm{H}}(\vec{\mathbf{r}}_0, \vec{\mathbf{r}}) \right\rangle$ represents the cross-spectral matrix, $(\cdot)^{\mathrm{H}}$ represents complex conjugate transposition, and $\langle \cdot \rangle$ represents the expected value. For convenience, Eq. (13) is denoted by MFP-B in the following sections.

The MV processor is one of the most commonly used adaptive array algorithms for MFP; it is designed to be optimum in the sense that the output noise power is minimized subject to the constraint that the signal is undistorted by the processor (Le Touze et al., 2012). The formulation of the MFP algorithm with the MV processor can be expressed as follows:

$$P_M(\vec{\mathbf{r}}_s, \vec{\mathbf{r}}) = \frac{1}{\mathbf{w}^{\mathrm{H}}(\vec{\mathbf{r}}_s, \vec{\mathbf{r}})\mathbf{K}^{-1}\mathbf{w}(\vec{\mathbf{r}}_s, \vec{\mathbf{r}})} \tag{14}$$

where $P_M(\vec{\mathbf{r}}_s, \vec{\mathbf{r}})$ is the output power of the MV processor and $(\cdot)^{-1}$ is the matrix inversion. For convenience, Eq. (14) is denoted by MFP-M in the following sections.

IV. SPARSE SIGNAL REPRESENTATION AND SOURCE LOCALIZATION WITH SPARSITY CONSTRAINT

In this section, we formulate the source localization problem as a sparse representation problem. For simplicity, first consider the single-snapshot scenario. Let $\{\vec{\mathbf{r}}_1, \vec{\mathbf{r}}_2, \ldots, \vec{\mathbf{r}}_m, \ldots, \vec{\mathbf{r}}_M\}$ (where $\vec{\mathbf{r}}_m$ belongs to the search grid area) be a sampling grid of all source locations of interest (Fig. 1); we can construct the sensing matrix $\mathbf{G}(\vec{\mathbf{r}}^{\mathrm{o}}, \vec{\mathbf{r}})$ by using Green's functions corresponding to each potential source location as its columns:

$$\mathbf{G}(\vec{\mathbf{r}}^{\mathrm{o}}, \vec{\mathbf{r}}) = \left[\boldsymbol{G}(\vec{\mathbf{r}}_1, \vec{\mathbf{r}}), \boldsymbol{G}(\vec{\mathbf{r}}_2, \vec{\mathbf{r}}), \ldots, \boldsymbol{G}(\vec{\mathbf{r}}_M, \vec{\mathbf{r}})\right] \tag{15}$$

where $\vec{\mathbf{r}}^{\mathrm{o}} = \left[\vec{\mathbf{r}}_1, \vec{\mathbf{r}}_2, \ldots, \vec{\mathbf{r}}_M\right]$ and $\mathbf{G}(\vec{\mathbf{r}}^{\mathrm{o}}, \vec{\mathbf{r}})$ is an overcomplete representation in terms of all possible source locations.

Consider K narrowband signals $s_k(t)$ (where k = 1, …, K) in the search grid area of interest, and reformulate the signals $s_k(t)$ using a new $M \times 1$ vector $\mathbf{S}(t)$, where the mth element $s_m(t)$ is nonzero and equal to $s_k(t)$ if source k is from $\vec{\mathbf{r}}_m$ for some k and is zero otherwise. The source localization problem is then recast as a sparse representation problem (Malioutov, 2011):

$$\mathbf{X}(t) = \mathbf{G}(\vec{\mathbf{r}}^{\mathrm{o}}, \vec{\mathbf{r}})\mathbf{S}(t) + \mathbf{N}(t) \tag{16}$$

where

$\mathbf{X}(t) = \left[x_1(t), x_2(t), \ldots, x_N(t)\right]^{\mathrm{T}}$ denotes sensor outputs;

$\mathbf{S}(t) = \left[s_1(t), s_2(t), \ldots, s_M(t)\right]^{\mathrm{T}}$ denotes sparse signal representation;

$\mathbf{N}(t) = \left[n_1(t), n_2(t), \ldots, n_N(t)\right]^{\mathrm{T}}$ denotes additive noise.

In general, the actual number of sources is small compared with all probable source locations of interest. Therefore, the underlying AMS for source localization is sparse, and Eq. (16) can be solved using the l_1-norm methodology, as described in Section II. In the presence of the noise field $N(t)$, Eq. (16) can be solved as follows (Edelmann and Gaumond, 2011):

$$\min \left\|\mathbf{S}(t)\right\|_1 \quad s.t. \quad \left\|\mathbf{G}(\vec{\mathbf{r}}^{\mathrm{o}}, \vec{\mathbf{r}})\mathbf{S}(t) - \mathbf{X}(t)\right\|_2 \le \varepsilon \tag{17}$$

where ε is the upper bound (or constraint parameter) for noise energy (l_2-norm). Eq. (17) represents the source localization

algorithm with the sparsity constraint in the ocean waveguide; for convenience, it is denoted by SLSC-I in the following sections.

In particular scenarios, including nonstationary sources, single-measurement processing may have advantages, and we can solve Eq. (17) for each measurement sequentially. However, for stationary sources, source localization estimation with multiple measurements is of relatively high practical importance and has the following form:

$$\mathbf{X}(t) = \mathbf{G}(\vec{\mathbf{r}}^{\,o}, \vec{\mathbf{r}})\mathbf{S}(t) + \mathbf{N}(t),\ t \in \{t_1, \ldots, t_T\} \tag{18}$$

Let $\mathbf{X} = [\mathbf{X}(t_1), \mathbf{X}(t_2), \ldots, \mathbf{X}(t_T)]$, $\mathbf{S} = [\mathbf{S}(t_1), \mathbf{S}(t_2), \ldots, \mathbf{S}(t_T)]$, and $\mathbf{N} = [\mathbf{N}(t_1), \mathbf{N}(t_2), \ldots, \mathbf{N}(t_T)]$. Eq. (18) can be further reformulated in a compact form as follows:

$$\mathbf{X} = \mathbf{G}(\vec{\mathbf{r}}^{\,o}, \vec{\mathbf{r}})\mathbf{S} + \mathbf{N} \tag{19}$$

The signal is generally sparse in space and not in time. Hence, determining the numerical solution to Eq. (19) is slightly complex. To address this concern, we should first compute the l_2-norm of all time samples of a particular spatial index of $\mathbf{S}$, such as $\mathbf{S}_i^{l_2} = \left\| [\mathbf{S}_i(t_1), \mathbf{S}_i(t_2), \ldots, \mathbf{S}_i(t_T)] \right\|_2$, and penalize the l_1-norm of $\mathbf{S}^{l_2} = \left[\mathbf{S}_1^{l_2}, \mathbf{S}_2^{l_2}, \ldots, \mathbf{S}_M^{l_2} \right]$ (Li and Zhang, 2015). Subsequently, Eq. (19) can be solved as follows:

$$\min \left\| \mathbf{S}^{l_2} \right\|_1 \quad s.t. \quad \left\| \mathbf{G}(\vec{\mathbf{r}}^{\,o}, \vec{\mathbf{r}})\mathbf{S} - \mathbf{X} \right\|_2 \le \sigma \tag{20}$$

where σ is the upper bound (or constraint parameter) for noise energy (l_2-norm). For convenience, Eq. (20), which deals with multiple snapshots, is denoted by SLSC-II in the following sections.

In practice, Eqs. (17) and (20) are convex optimization problems and can be readily addressed using various tools, such as the l_1-MAGIC package (Candès and Romberg, 2015), SeDuMi software (Sturm, 1999), and CVX toolbox (Boyd and Vandenberghe, 2004). In this study, we proposed the use of the CVX toolbox, which can solve considerably more complex convex optimization problems, including several problems with non-differentiable functions, such as l_1-norms compared with other tools (Grant and Boyd, 2015).

In summary, the procedure for implementing our proposed algorithm (or obtaining the solution) is summarized as follows:

(1) Discretize the observable space and determine a sampling grid of all source locations of interest.
(2) According to Eq. (15), construct the sensing matrix $\mathbf{G}(\vec{\mathbf{r}}^{\,o}, \vec{\mathbf{r}})$ by using Green functions corresponding to each potential source location as its columns.
(3) Acquire the sensor outputs and form the array data samples $\mathbf{X}(t)$ or $\mathbf{X} = [\mathbf{X}(t_1), \mathbf{X}(t_2), \ldots, \mathbf{X}(t_T)]$. If the algorithm SLSC-I is selected, proceed to Step (4). If algorithm SLSC-II is selected, proceed to Step (5).
(4) According to Eq. (17), set the constraint parameter ε and call the CVX toolbox to seek $\mathbf{S}(t)$ that minimizes $\left\| \mathbf{S}(t) \right\|_1$ under the constraint condition $\left\| \mathbf{G}(\vec{\mathbf{r}}^{\,o}, \vec{\mathbf{r}})\mathbf{S}(t) - \mathbf{X}(t) \right\|_2 \le \varepsilon$. proceed to Step (6).
(5) According to Eq. (20), set the constraint parameter σ and call the CVX toolbox to seek $\mathbf{S}$ that minimizes $\left\| \mathbf{S}^{l_2} \right\|_1$ under the constraint condition $\left\| \mathbf{G}(\vec{\mathbf{r}}^{\,o}, \vec{\mathbf{r}})\mathbf{S} - \mathbf{X} \right\|_2 \le \sigma$.
(6) Finally, compute the signal energy from different sampling grids of all source locations of interest and present an ambiguity surface. Subsequently, define the location estimates for the acoustic sources by using the location of the largest peaks on the ambiguity surface.

V. NUMERICAL RESULTS OBTAINED USING SYNTHETIC DATA

This section details computer simulations conducted to evaluate the performance of our proposed algorithm. The signal-to-noise ratio (SNR) array for a single array measurement is defined in decibels as follows:

$$\mathrm{SNR} = 20\log_{10}\left(\frac{\left\| \mathbf{G}(\vec{\mathbf{r}}^{\,o}, \vec{\mathbf{r}})\mathbf{S}(t) \right\|_2}{\left\| \mathbf{N}(t) \right\|_2} \right) \tag{21}$$

1. AMS for Coherent Source Localization in Ocean Waveguide

First, we considered a coherent source localization example in a complex ocean environment with a depth-varying sound speed profile. Such environments are appropriate for demonstrating the performance of the proposed algorithm.

The ocean profile was converted into one involving three piecewise linear segments, defining a double-duct profile (Fig. 2). The sound speed varied from 1500 m/s (at the surface and at a depth of 3000 m) to 1550 m/s (at a depth of 1000 m and at the bottom, which was assumed to be at a depth of 5000 m). The bottom was determined to be fluid with a sound speed of 2000 m/s and a density of 2.0 g/cm^3. Two coherent acoustic sources were observed in this horizontally stratified ocean. One source was located at a depth of 150 m and a range of 180 km from a vertical line array (VLA), whereas the other was at a depth of 230 m and a range of 130 km. The VLA was a 19-element array of hydrophones spaced at 50 m, and the uppermost element was at a depth of 55 m; thus, the total length of the array was 900 m. The field at the hydrophones was calculated at a frequency of 10 Hz by using an NM propagation model. Specifically, 42 modes were available for the double-duct problem solved using the numerical code Kraken. However, for simplicity, only the

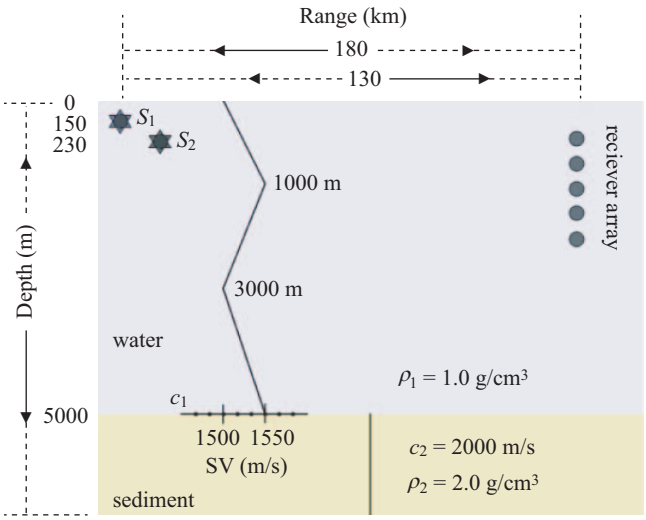

Fig. 2. Ocean waveguide with double-duct profile.

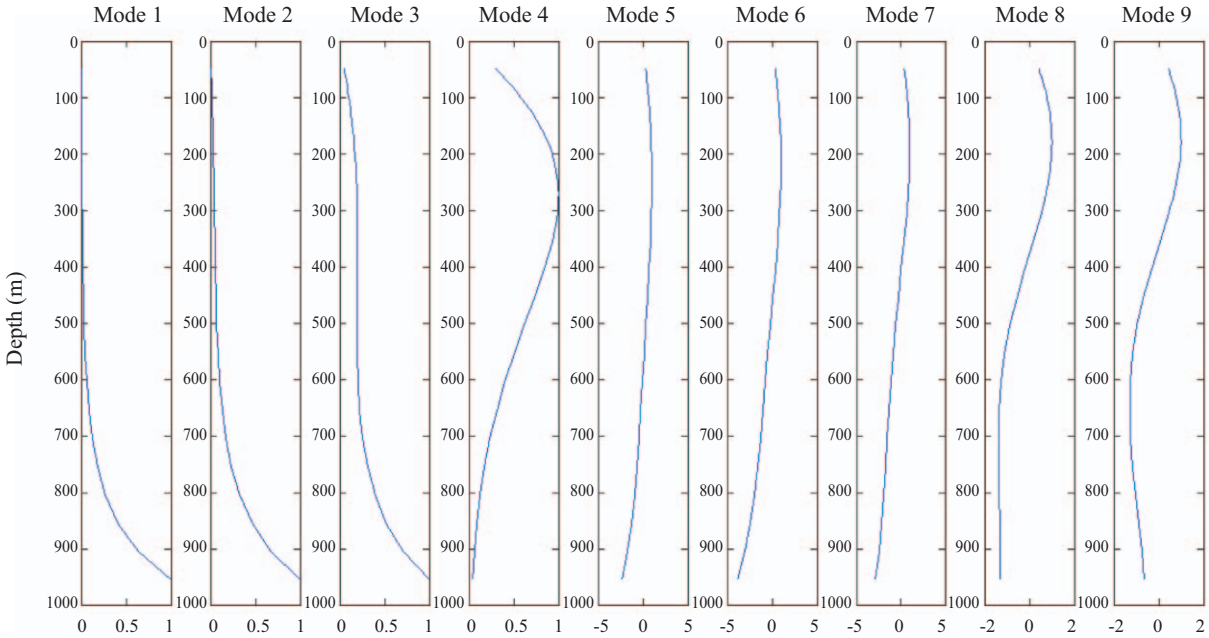

Fig. 3. First nine modes for double-duct problem.

first nine modes are plotted in Fig. 3.

The SNR was set to 20 dB (upper bound $\varepsilon = 1\times10^{-5}$ and $\sigma = 1\times10^{-5}$). The total number of multiple measurements was 16. The numerical search grid for localization spanned from 100 to 220 km, with a 1-km spacing in range, and from 50 to 290 m, with a 10-m spacing in depth. Fig. 4 illustrates the normalized AMS results from all three processors with a single snapshot and multiple snapshots.

The Bartlett processor is robust to a small training sample size. Therefore, the AMS results from the processes with the single snapshot and multiple snapshots were approximately the same, as illustrated in Figs. 4(a) and 4(b), respectively. However, several high sidelobes were observed. MFP-B displayed strong ambiguities competing with the true source positions. Figs. 4(c) and 4(d) present the AMS results from MFP-M with a single snapshot and multiple snapshots, respectively. Figs.4(c) and 4(d) are considerably different. Typically, a small training sample size engenders a considerable degradation of the performance of the MV processor, and this thus explains the difference between the two figures. As shown in Fig. 4(c), noise interfered with the two coherent signals, preventing these signals from being distinguished. Fig. 4(d) indicates a high-level pseudo-peak, signifying a false target (i.e., a point of the highest power indicated by an arrow). Hence, in this scenario, MFP-B and MFP-M could not perform adequately in capturing signals and precisely locating the sources. Finally, the results

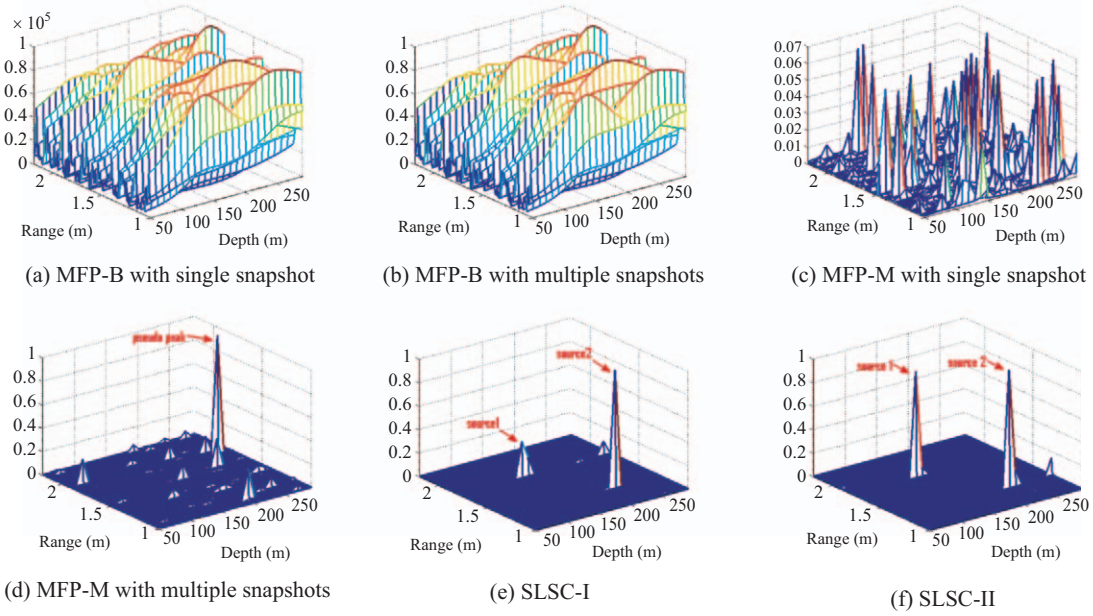

(a) MFP-B with single snapshot (b) MFP-B with multiple snapshots (c) MFP-M with single snapshot

(d) MFP-M with multiple snapshots (e) SLSC-I (f) SLSC-II

Fig. 4. AMS results observed for all three processors.

in Figs. 4(e) and 4(f) are consistent with the proposed theoretical arguments associated with Eqs. (17) and (20), describing the sparsity-constraint properties of SLSC-type algorithms. As shown in Fig. 4(e), SLSC-I could suppress all noise and precisely locate coherent sources. However, the actual estimated amplitudes of the two coherent sources were considerably different (i.e., one was approximately 0.2, whereas the other was nearly 0.8). In contrast to SLSC-I, SLSC-II had two separated large peaks, which were considerably sharper and more focused at the accurate source positions (indicated using arrow), as presented in Fig. 4(f). For multiple snapshots, SLSC-II could evidently discern the two closely spaced sources. Accordingly, the numerical simulation results indicate that the SLSC-type algorithms could perform adequately in localizing coherent sources in the complex ocean environment with a depth-varying sound speed profile and could provide higher resolution than could MFP-B and MFP-M.

2. Source Localization Performance versus SNR

In previous sections, we analyze AMS results for MFP-B, MFP-M, SLSC-I, and SLSC-II. Source localization performance is highly dependent on the SNR at a receiving array. Accordingly, from a statistical perspective, we closely investigated the performance of the aforementioned algorithms by considering source localization with varying SNRs. Source localization performance was determined to be based on the source localization error (SLE) and mainlobe-to-sidelobe ratio (MSR), where SLE is defined as the Euclidean distance:

$$\mathrm{SLE} = \sqrt{\left(r_0 - r_{peak}\right)^2 + \left(z_0 - z_{peak}\right)^2} \tag{22}$$

where r_0 and z_0 represent the range and depth of the true source, respectively, whereas r_{peak} and z_{peak} represent the range and depth of the highest peak in AMS, respectively. In addition, the MSR is defined as follows:

$$\mathrm{MSR} = 20\log_{10}\left(\frac{P_{peak}}{P_{max\text{-}sidelobe}}\right) \tag{23}$$

where P_{peak} and $r_{max\text{-}sidelobe}$ represent the power of the highest peak and power of the maximum sidelobe in AMS, respectively.

Consider the Pekeris waveguide in Fig. 5. The waveguide for this numerical simulation was range-independent with a bottom depth of 1000 m and had a homogeneous fluid layer with a sound speed of 1500 m/s overlying a bottom with a sound speed of 2000 m/s and density of 2.0 g/cm^3. The acoustic source was located at a depth of 150 m and a range of 180 km from the VLA. The VLA was a 19-element array of hydrophones spaced at 50 m, and the uppermost element was at a depth of 55 m; therefore, the total length of the array was 900 m. The replica search grid for localization extended from 100 to 220 km, with a 1-km spacing in range, and from 100 to 290 m, with a 10-m spacing in depth. The VLA data were generated at a frequency of 10 Hz by using an NM propagation model.

In the scenario involving a single snapshot, the constraint parameter was set to $\varepsilon = 1 \times 10^{-5}$, SNR changed from -10 to 30 dB, and number of Monte Carlo trials was 200 (each point in the plot represents the average of 200 trials). Fig. 6 presents a comparison of the numerical results obtained using MFP-B, MFP-M, and SLSC-I with a single snapshot.

Fig. 6(a) provides a comparison of the three processors in terms of the SLE as a function of SNR. The numerical results for all three processors improved as the SNR increased, although some

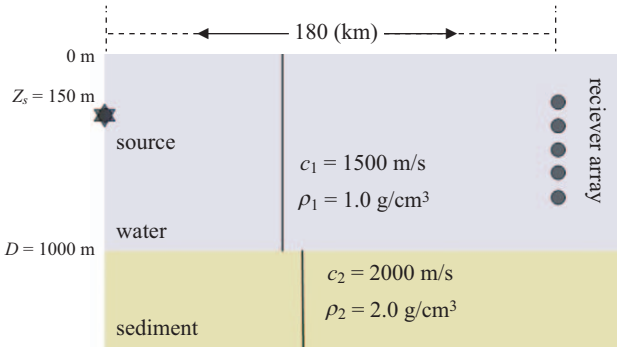

Fig. 5. Pekeris waveguide with environmental parameters.

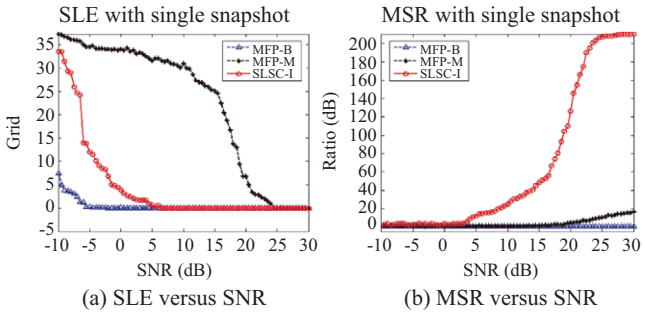

Fig. 6. SLE and MSR versus SNR in scenario involving single snapshot.

processor results were determined to asymptote to an approximately constant value at higher SNRs. For example, the SLE for MFP-M, MFP-B, and SLSC-I was approximately 0 at the SNRs of more than 24, 5, and -5 dB, respectively. The performance of MFP-B and SLSC-I was considerably superior to that of MFP-M at intermediate SNRs, (where the SNR varied from 5 to 24 dB). However, when the SNR was less than 5 dB, the performance of SLSC-I was slightly worse than that of MFP-B. Fig. 6(b) shows a comparison of the performance of the three processors in terms of the MSR versus SNRs. At lower SNRs (where the SNR varied from -10 to 4 dB), the MSRs for all three processors were approximately 0. When the SNR was higher than 4 dB, the MSR increased with the SNR for all processors. SLSC-I outperformed MFP-B and MFP-M, whereas MFP-M performed slightly better than MFP-B at higher SNRs, with significant differences (MSR of ~ 20 dB) when the SNR was 30 dB.

In the scenario involving multiple snapshots, the constraint parameter was set to $\sigma = 1\times10^{-4}$, SNR was varied from -10 to 10 dB, and number of Monte Carlo trials was 200 (each point in the plot represents the average of 200 trials). Fig. 7 illustrates the numerical results obtained using MFP-B, MFP-M, and SLSC-II with multiple snapshots.

The results in Fig. 7 are similar to those in Fig. 6. As shown in Fig. 7(a), the performance of MFP-B and SLSC-II was considerably superior to that of MFP-M overall, whereas the performance of SLSC-II was slightly worse than that of MFP-B at lower SNRs (SLE differences of approximately 2 grids at an SNR of -6 dB). As illustrated in Fig. 7(b), the MSR performance of

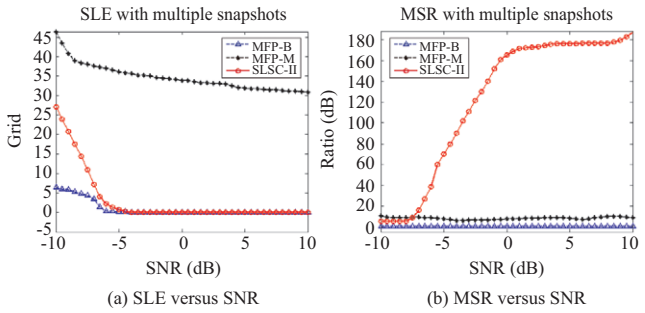

Fig. 7. SLE and MSR versus SNR in scenario involving multiple snapshots.

SLSC-II improved with the decreasing noise. Furthermore, SLSC-II outperformed MFP-B and MFP-M overall, whereas the MSR of MFP-M was higher than that of MFP-B by nearly 10 dB. However, in contrast to the scenario involving the single snapshot, the performance of the SLSC-type algorithms was significantly improved in the scenario involving multiple snapshots, as shown in Fig. 7. For example, SLSC-II had an SLE of approximately 0 grids and MSR of 170 dB at an SNR of 0 dB, whereas SLSC-I had an SLE of approximately 3 grids and an MSR of 0 dB. Moreover, the snapshot number had almost no influence on MFP-B.

On the basis of the results presented in this section, we can conclude that the SLSC-type algorithms exhibited a considerably higher resolution (i.e., lower SLE and higher MSR) and higher performance than did MFP-B and MFP-M provided that scenarios were appropriately conditioned (i.e., preventing excessively low SNRs, such as lower than 5 dB in the scenario involving the single snapshot and lower than -4 dB in that involving multiple snapshots).

3. Influence of Model Mismatch

Previous studies have indicated that a major limitation of source localization in the ocean waveguide is sensitivity to model mismatches that occur when an inaccurate model is established for the ocean waveguide (e.g., sound speed profile errors, channel depth errors, and sensor position errors) (Bilik, 2011). The aforementioned scenarios did not consider the mismatch between the propagation environment and the adopted acoustic model. However, in practical applications, uncertainties in model parameter values must be addressed. An underwater source localization algorithm utilizes information on the environment by using Green's functions. Green's functions contain all information on an underwater sound propagation environment or channel. Green's functions are functions of underwater sound propagation environments or channel parameters. If these parameters are erroneous or affected by interference (or the underwater environment includes a model mismatch), Green's function perturbation occurs. Therefore, the model mismatch can be defined by using Green's function perturbation. Moreover, its influence on source localization performance can be further studied. The model mismatch is defined as follows:

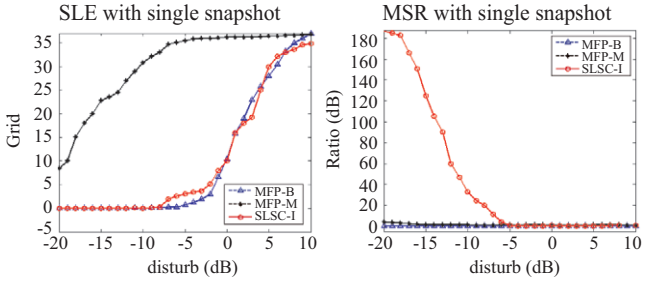

(a) SLE versus model mismatch (b) MSR versus model mismatch

Fig. 8. SLE and MSR versus model mismatch in scenario involving single snapshot.

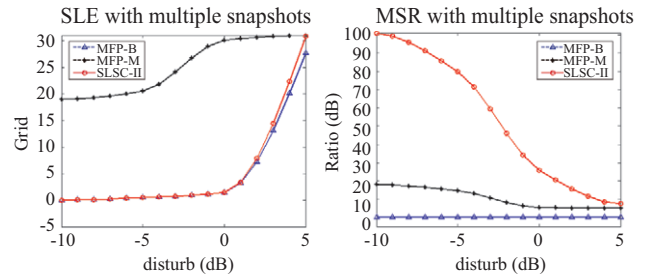

(a) SLE versus model mismatch (b) MSR versus model mismatch

Fig. 9. SLE and MSR versus model mismatch in scenario involving multiple snapshots.

$$10\log_{10}\left(\frac{\left\|\Delta\mathbf{G}(\vec{\mathbf{r}}_0,\vec{\mathbf{r}})\right\|_F^2}{\left\|\mathbf{G}(\vec{\mathbf{r}}_0,\vec{\mathbf{r}})\right\|_F^2}\right) \tag{24}$$

where $\|\cdot\|_F$ and $\Delta\mathbf{G}(\vec{\mathbf{r}}_0,\vec{\mathbf{r}})$ denote Frobenius norm and Green's function perturbation, respectively.

To illustrate the influence of model mismatch, we compared the performance of all three processors against different model mismatches, as illustrated in Figs. 8 and 9, which respectively correspond to a single snapshot and multiple snapshots. As shown in Fig. 8, the simulation condition was the same as that described in Section 5.2, except that the model mismatch changed from -20 to 10 dB. The acoustic source was located at a depth of 150 m and a range of 180 km from the VLA, and the number of Monte Carlo trials was 200.

As the model mismatch increased, the SLEs for all processors increased and the MSRs decreased (Fig. 8). Previous studies on MFP have indicated the robustness of MFP-B to model mismatches (Kuperman and Song, 2012). As expected, MFP-B had the lowest SLEs overall. SLSC-I was comparable to MFP-B at a low model mismatch (i.e., less than -8-dB disturbance, as shown Fig. 8(a)); however, its performance was slightly worse at higher model mismatches (i.e., more than -8-dB disturbance). MFP-M was highly sensitive to the model mismatch and exhibited the worst performance of all processors. When the disturbance was -10 dB, MFP-B and SLSC-I exhibited accurate source localization results (an SLE of approximately 0 grids, as shown in Fig. 8(a)), whereas MFP-M had an SLE of 30 grids. In addition, Fig. 8(b) illustrates plots of the MSR against model mismatch. When the model mismatch was lower than -5 dB, SLSC-I evidently outperformed MFP-B and MFP-M. However, when the model mismatch was higher than -5 dB, all three processors exhibited the same MSR (approximately equal to 0 dB).

Fig. 9 shows the results for the scenario involving multiple snapshots. The simulation conditions were the same as those in the preceding scenario, except that the model mismatch changed from -10 to 5 dB, and the number of Monte Carlo trials was 200.

As presented in Fig. 9(a), MFP-B and SLSC-II exhibited considerably lower SLEs than did MFP-M for lower model mismatches (where the disturbance was less than 0 dB). However, when the model mismatches were higher than 0 dB, MFP-B and SLSC-II exhibited performance degradations. Fig. 9(b) presents plots of the MSR versus model mismatch. As the model mismatch increased, the MSR observed for SLSC-II decreased but was considerably higher than those observed for the MFP-B and MFP-M when the disturbance was lower than 0 dB. Therefore, the simulation figures indicate the robustness of SLSC-II to model mismatches, representing that SLSC-II is less sensitive to model mismatches for disturbances of less than 0 dB.

The simulation results in this subsection clearly demonstrate the superior performance of the SLSC-type algorithms (i.e., high robustness to model mismatches), obtained by utilizing information from the sparsity constraint, compared with MFP-B and MFP-M.

4. Source Localization Performance versus Constraint Parameter

The preceding numerical results were obtained under the condition of fixed constraint parameters. However, the advantages of SLSC-type algorithms can only be materialized if appropriate constraint parameters are selected. Selecting appropriate constraint parameters is crucial in practical applications. From a statistical perspective, we evaluated the performance of the SLSC-type algorithms by considering source localization under different constraint parameters.

The simulation condition was the same as those described in Section 5.2, except that the constraint parameter ε was changed from 0.5×10^{-5} to 5×10^{-5}. Fig. 10 shows the numerical results observed for SLSC-I. The curves are labeled with different SNRs in decibels. Each curve varies with respect to two parameters, namely a constraint parameter corresponding to the horizontal axis and the SNR value.

Fig. 10(a) illustrates plots of the SLE as a function of the constraint parameter at a fixed SNR. At intermediate parameters, where the constraint parameter was varied from 0.8×10^{-5} to 3.5×10^{-5}, SLSC-I had a low SLE and high overall performance. This signifies that localization accuracy was achieved in this range of constraint parameters, which can be termed the *confidence interval* indicated by the two vertical dashed lines. However, when the parameters were higher than

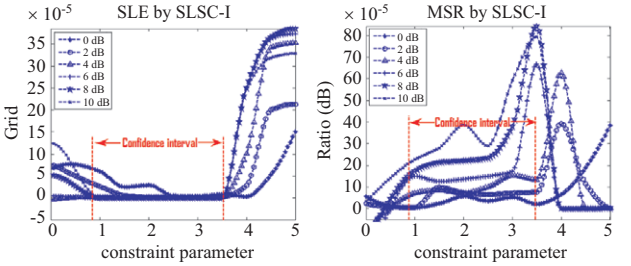

(a) SLE versus constraint parameter (b) MSR versus constraint parameter

Fig. 10. SLE and MSR versus constraint parameter for SLSC-I.

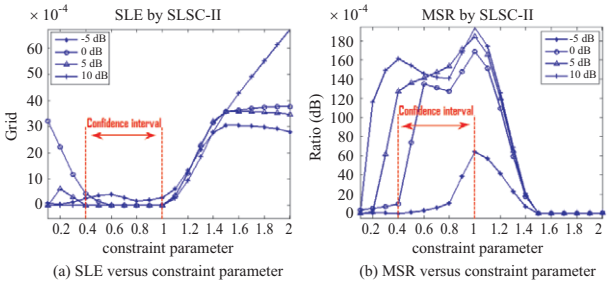

(a) SLE versus constraint parameter (b) MSR versus constraint parameter

Fig. 11. SLE and MSR versus constraint parameter for SLSC-II.

3.5×10^{-5}, the SLE became higher and performance degradation occurred. Fig. 10(b) presents plots of the MSR against the constraint parameter at a fixed SNR. At intermediate parameters, where the parameter was varied from 0.8×10^{-5} to 3.5×10^{-5}, a higher SNR indicated a higher MSR. However, when the parameter was higher than 3.5×10^{-5}, the simulation results were invalid because of inaccurate localization results (Fig. 10(a)). Therefore, these results demonstrate that accurate localization depends on the parameter choice or confidence intervals (i.e., from 0.8×10^{-5} to 3.5×10^{-5} under this simulation condition).

Fig. 11 shows the numerical results observed for SLSC-II. The simulation conditions were the same as the mentioned conditions, except that the constraint parameter σ was changed from 1×10^{5} to 2×10^{-4}. The confidence interval could be defined from 0.4×10^{-4} to 1×10^{-4}, as indicated by the two vertical dashed lines (Fig. 11). In this confidence interval, SLSC-II achieved a lower SLE and higher MSR than those in other intervals. As the SNR increased, performance was improved. For example, SLSC-II exhibited a higher MSR at an SNR of 0 dB than it did at an SNR of -5 dB (Fig. 11(b)). SLSC-II performed appropriately when the parameter was selected from the confidence interval (i.e., from 0.4×10^{-4} to 1×10^{-4}).

The simulation results presented in this section demonstrate the superior performance of the SLSC-type algorithms, which could be achieved by selecting the appropriate confidence interval. The confidence interval can be specified under certain simulation conditions and can be used as a guide to parameter section.

VI. CONCLUSION

This paper proposes a robust super-resolution source localization approach in an ocean waveguide. The proposed technique explicitly applies the inherent sparse structure of the localization problem and underwater sound propagation model to achieve a relatively high spatial resolution. Moreover, the proposed approach can be formulated as a sparse representation problem and further converted into a convex optimization problem with a sparsity constraint, which can be efficiently solved using the CVX toolbox. Computer simulations were conducted to compare the AMS results in several frequently encountered situations, such as single source localization, coherent source localization, and targets outside the area of interest. In addition, the effect of the SNR, constraint parameters, and model mismatch on source localization performance was thoroughly analyzed using numerical simulations. In summary, the numerical simulation results indicate that the proposed SLSC-type algorithms (i) can perform well in source localization in the ocean waveguide, (ii) are highly robust to model mismatches, and (iii) have considerably higher resolution (lower SLE and higher MSR) than do the available conventional methods under appropriate conditions and appropriate confidence intervals of constraint parameters.

ACKNOWLEDGEMENTS

This work was supported by the Fund for Young Fostering Talents of the Higher Education Institutions in Heilongjiang Province in 2015 (Grant No. UNPYSCT-2015101), the Natural Science Foundation for Outstanding Young Talents of Heilongjiang Province and the Fundamental Research Funds for the Universities of Education Department of Heilongjiang Province (Innovative Research Team: Grant No. 2018CX11).

REFERENCES

Baggeroer, A. B., W. A. Kuperman and P. N. Mikhalevsky (1993). Overview of matched field methods in ocean acoustics. IEEE Journal of Oceanic Engineering, Vol. 18, No. 4, 401-424.

Baraniuk, R. G. (2007). Compressive sensing. IEEE Signal Processing Magazine, Vol. 24, No. 4, 118-124.

Bilik, I. (2011). Spatial Compressive sensing for direction-of-arrival estimation of multiple sources using dynamic sensor arrays. IEEE Transactions on Aerospace and Electronic Systems, Vol. 47, No. 3, 1754-1769.

Boyd, S. and L. Vandenberghe (2004). Convex Optimization. Cambridge University Press, New York.

Candès, E. J., J. Romberg and T. Tao (2006). Robust uncertainty principles: Exact signal reconstruction from highly incomplete frequency information. IEEE Transactions on Information Theory, Vol. 52, No. 2, 489-509.

Candès, E. J. and J. Romberg (2015). l_1-magic: Recovery of sparse signals via convex programming. http://statweb.stanford.edu/~candes/l1magic/#code (last viewed July 31, 2015)

Candes, E. J. and M. B. Wakin (2008). An introduction to compressive sampling. IEEE Signal Processing Magazine, Vol. 25, No. 2, 21-30.

Chang, S. H., J. C. Liu and C. W. Chiu (2001). Applying time-frequency distribution function to DOA of mobile active sensor. Journal of Marine Science and Technology, Vol. 9, No. 2, 161-166.

Donoho, D. L. (2006). Compressed sensing. IEEE Transactions on Information Theory, Vol. 52, No. 4, 1289-1306.

Dosso, S. E. and M. J. Wilmut (2013). Bayesian tracking of multiple acoustic

sources in an uncertain ocean environment. The Journal of the Acoustical Society of America, Vol. 133, No. 4, 274-280.

Edelmann, G. F. and C. F. Gaumond (2011). Beamforming using compressive sensing. The Journal of the Acoustical Society of America, Vol. 130, No. 4, 232-237.

Eldar, Y. C. and G. Kutyniok (2012). Compressed Sensing: Theory and Applications. Cambridge University Press, New York.

Etter, P. C. (2013). Underwater Acoustic Modeling and Simulation. CRC Press, New York.

Forero, P. A. and P. A. Baxley (2014). Shallow-water sparsity-cognizant source-location mapping. The Journal of the Acoustical Society of America, Vol. 135, No. 6, 3483-3501.

Gorodnitsky, I. F. and B. D. Rao (1997). Sparse signal reconstruction from limited data using FOCUSS: A re-weighted minimum norm algorithm. IEEE Transactions on Signal Processing, Vol. 45, No. 3, 600-616.

Grant, M. and S. Boyd (2015). CVX: Matlab software for disciplined convex programming, version 2.0 beta. http://cvxr.com/cvx (Last viewed July 31, 2015).

Hou, S. Y., S. H. Chang, H. S. Hung and J. Y. Chen (2009). DSP-based implementation of a real-time DOA estimator for underwater acoustic sources. Journal of Marine Science and Technology, Vol. 17, No. 4, 320-325.

Jensen, F. B., W. A. Kuperman, M. B. Porter and H. Schmidt (2011). Computational Ocean Acoustics. New York, Springer.

Jiang, L., R. He, Y. Hong, J. Wu and H. Shu (2017a). Active wideband higher-order raypath separation in multipath environment. The Journal of the Acoustical Society of America, Vol. 141, No. 1, EL38-EL44.

Jiang, L., R. He, Y. Hong, J. Wu and H. Shu (2017b). Two-dimensional active raypath separation using examination of the roots of the spectrum polynomial. The Journal of the Acoustical Society of America, Vol. 142, No. 4, EL408-EL414.

Jiang, L., W. Song, Z. Zhang, C. Yang, S. Wang and P. Roux (2017). Fast raypath separation based on low-rank matrix approximation in a shallow-water waveguide. The Journal of the Acoustical Society of America, Vol. 143, No. 4, EL271-EL277.

Kuperman, W. A. and H. C. Song (2012). Integrating ocean acoustics and signal processing. In: AIP Conference Proceedings, Beijing, China, 69-82.

Le Touze, G., B. Nicolas, J. I. Mars, P. Roux and B. Oudompheng (2012). Double-capon and double-musical for arrival separation and observable estimation in an acoustic waveguide. EURASIP Journal on Advances in Signal Processing, Vol. 2012, No. 1, p.187.

Li, Y. and G. Zhang (2015). A seismic blind deconvolution algorithm based on bayesian compressive sensing. Mathematical Problems in Engineering, 427153.

Malioutov, D., M. Çetin and A. S. Willsky (2005). A sparse signal reconstruction perspective for source localization with sensor arrays. IEEE Transactions on Signal Processing, Vol. 53, No. 8, 3010-3022.

Malioutov, D. (2011). A sparse signal reconstruction perspective for source localization with sensor arrays. B.S. Thesis, Electrical and Computer Engineering Northeastern University, Massachusetts Institute of Technology, USA.

Mantzel, W., J. Romberg and K. Sabra (2012). Compressive matched-field processing. The Journal of the Acoustical Society of America, Vol. 132, No. 1, 90-102.

Orović, I., V. Papić, C.Ioana, X. Li and S. Stanković (2016). Compressive sensing in signal processing: algorithms and transform domain formulations. Mathematical Problems in Engineering, 7616393.

Rossi, M., A. M. Haimovich and Y. C. Eldar (2014). Spatial compressive sensing for MIMO radar. IEEE Transactions on Signal Processing, Vol. 62, No. 2, 419-430.

Schmidt, H. and F. B. Jensen (2012). Computational ocean acoustics: Advances in 3D ocean acoustic modeling. In: AIP Conference Proceedings, Beijing, China, 3-15.

Shi, J., D. S. Yang and S. G. Shi (2011a). Robust localization and identification method of moving sound sources based on worst-case performance optimization. Acta Physica Sinica, Vol. 60, No. 6, 064301.

Shi, J., D. S. Yang and S. G. Shi (2011b). A robust localization and identification method of noise sources using second-order cone programming. Journal of Harbin Engineering University, Vol. 32, No. 12, 1549-1555.

Shi, J., D. S. Yang and S. G. Shi, (2011c). Near-field source localization algorithm based on the combination array. Acta Electronica Sinica, Vol. 39, No. 6, 1231-1237.

Shi, J., D. S. Yang and S. G. Shi, (2012). Experimental research on cylindrical focused beamforming localization method of moving sound sources based on vector sensor array. Acta Physica Sinica, Vol. 61, No. 12, 124302.

Si, W., X. Qu, Y. Jiang and T. Chen (2015). Multiple sparse measurement gradient reconstruction algorithm for DOA Estimation in compressed sensing. Mathematical Problems in Engineering, 152570.

Somasundaram, S. D., N. H. Parsons, P. Li and R. C. Lamare (2015). Reduced-dimension robust capon beamforming using Krylov-subspace techniques. IEEE Transactions on Aerospace and Electronic Systems, Vol. 51, No. 1, 270-289.

Song, H. Y., J. Shi, C. Y. Yang, B. S. Liu and M. Diao (2015). Robust bearing estimation in shallow water using vector optimization. Journal of Marine Science and Technology, Vol. 23, No. 2, 151-161.

Sturm, J. F. (1999). Using Sedumi 1.02, a MATLAB toolbox for optimization over symmetric cones. Optimization Methods and Software, Vol. 11, No. 1, 625-653.

Tolstoy, A. (1993). Matched field processing for underwater acoustics. World Scientific Publishing, Singapore.

Xenaki, A., P. Gerstoft and K. Mosegaard (2014). Compressive beamforming. The Journal of the Acoustical Society of America, Vol. 136, No. 1, 260-271.

Yang, T. C (2014). Data-based matched-mode source localization for a moving source. The Journal of the Acoustical Society of America, Vol. 135, No. 3, 1218-1230.

Yin, M., K. Yu and Z. Wang (2016). Compressive Sensing Based Sampling and Reconstruction for Wireless Sensor Array Network. Mathematical Problems in Engineering, 9641608.

Zhang, L., Z. Zhu, B. Yang, W. Liu, H. Zhu and M. Zou (2015). Medical image encryption and compression scheme using compressive sensing and pixel swapping based permutation approach. Mathematical Problems in Engineering, 940638.